Remote Sensing of Environment 113 (2009) 2463–2475

Contents lists available at ScienceDirect

Remote Sensing of Environment

journal homepage: www.elsevier.com/locate/rse

An assessment of photosynthetic light use efficiency from space: Modeling the atmospheric and directional impacts on PRI reflectance

Thomas Hilker [a,*], Alexei Lyapustin [b,c], Forrest G. Hall [d,e], Yujie Wang [a,b], Nicholas C. Coops [a], Guillaume Drolet [f], T. Andrew Black [g]

[a] Faculty of Forest Resources Management, University of British Columbia, 2424 Main Mall, Vancouver BC, Canada V6T 1Z4
[b] University of Maryland, Baltimore County, 1000 Hilltop Circle, Baltimore, MD 21250, USA
[c] NASA Goddard Space Flight Center, Code 614.4, Greenbelt Maryland, 20771, USA
[d] Joint Center for Earth Systems Technology, University of Maryland, Baltimore County, USA
[e] Goddard Space Flight Center, Greenbelt Maryland, 20771, Code 614.4, USA
[f] Faculté de foresterie et de géomatique, Pavillon Abitibi-Price, Université Laval, Québec, QC, Canada G1V 0A6
[g] Faculty of Land and Food Systems, University of British Columbia, 2357 Main Mall, Vancouver, BC, Canada V6T 1Z4

ARTICLE INFO

Article history:
Received 15 March 2009
Received in revised form 2 June 2009
Accepted 18 July 2009

Keywords:
Photosynthesis
Carbon cycling
PRI
Remote sensing
MAIAC
6S
Atmospheric correction
Multi-angular
BRDF
Eddy covariance
MODIS
Upscaling
Photochemical reflectance index
AMSPEC
LiDAR
Hyperspectral
Spectroradiometer
Flux tower
Global carbon cycle
Douglas fir

ABSTRACT

Estimation of photosynthetic light use efficiency (ε) from satellite observations is an important component of climate change research. The photochemical reflectance index, a narrow waveband index based on the reflectance at 531 and 570 nm, allows sampling of the photosynthetic activity of leaves; upscaling of these measurements to landscape and global scales, however, remains challenging. Only a few studies have used spaceborne observations of PRI so far, and research has largely focused on the MODIS sensor. Its daily global coverage and the capacity to detect a narrow reflectance band at 531 nm make it the best available choice for sensing ε from space. Previous results however, have identified a number of key issues with MODIS-based observations of PRI. First, the differences between the footprint of eddy covariance (EC) measurements and the MODIS footprint, which is determined by the sensor's observation geometry make a direct comparison between both data sources challenging and second, the PRI reflectance bands are affected by atmospheric scattering effects confounding the existing physiological signal. In this study we introduce a new approach for upscaling EC based ε measurements to MODIS. First, EC-measured ε values were "translated" into a tower-level optical PRI signal using AMSPEC, an automated multi-angular, tower-based spectroradiometer instrument. AMSPEC enabled us to adjust tower-measured PRI values to the individual viewing geometry of each MODIS overpass. Second, MODIS data were atmospherically corrected using a Multi-Angle Implementation of Atmospheric Correction (MAIAC) algorithm, which uses a time series approach and an image-based rather than pixel-based processing for simultaneous retrievals of atmospheric aerosol and surface bidirectional reflectance (BRDF). Using this approach, we found a strong relationship between tower-based and spaceborne reflectance measurements ($r^2 = 0.74$, $p < 0.01$) throughout the vegetation period of 2006. Swath (non-gridded) observations yielded stronger correlations than gridded data ($r^2 = 0.58$, $p < 0.01$) both of which included forward and backscatter observations. Spaceborne PRI values were strongly related to canopy shadow fractions and varied with different levels of ε. We conclude that MAIAC-corrected MODIS observations were able to track the site-level physiological changes from space throughout the observation period.

1. Introduction

Remote sensing of plant photosynthesis using satellite observations will greatly enhance our understanding of the terrestrial carbon cycle, as it allows a spatially continuous estimate of plant CO_2 uptake on a global scale (Comins & McMurtrie 1993; Field et al., 1992). Plants absorb CO_2 from the atmosphere through photosynthesis, also known as gross primary production (GPP), and release it back into the atmosphere through respiration and decomposition of dead organic matter. The rate of carbon absorption is proportional to product of the incident photosynthetically active radiation (the radiation between 400 and 700 nm wavelength, PAR), the fraction of PAR absorbed by the green canopy elements (f_{PAR}) and the efficiency ε (g C MJ^{-1}) with which the absorbed PAR is used to produce biomass, also known as light use efficiency (Monteith 1972, 1977). This light use efficiency is controlled by any of a large factors restraining the photochemical

* Corresponding author. Tel.: +1 604 827 4429; fax: +1 604 822 9106.
E-mail address: thomas.hilker@ubc.ca (T. Hilker).

0034-4257/$ – see front matter © 2009 Elsevier Inc. All rights reserved.
doi:10.1016/j.rse.2009.07.012

reaction process, such as temperature, nutrient and water supply and, as a result, varies greatly in space and time (Field & Mooney 1986, Prince & Goward 1995, Turner et al., 2003).

In recent decades, we have seen considerable progress in determining PAR and f_{PAR} on global scales using satellite observations (Asrar et al., 1984; Chen et al., 1997; Daughtry et al., 1983; Sellers, 1985; Sellers, 1987; Tucker, 1979), however, direct estimation of ε remains challenging. Current GPP models often incorporate ε by using meteorological variables to estimate stress related restrictions to the photochemical reaction chain (Heinsch et al., 2006; Prince & Goward 1995; Running et al., 2004b; Sellers et al., 1996). The accuracy of this approach however, is limited by a lack of detailed knowledge of stressors at landscape and global scales (Collelo et al., 1998; Heinsch et al., 2006; Martel et al., 2005). As an alternative to determining ε from environmental stresses, Gamon et al. (1993) and Gamon et al. (1992) introduced the photochemical reflectance index (PRI), a narrow waveband index that relates ε to a xanthophyll-induced absorption feature at 531 nm, which is directly linked to the biochemical mechanism down-regulating photosynthesis to prevent photo-oxidative damage in leafs (Demmig-Adams & Adams 1996):

$$\mathrm{PRI} = \frac{\rho_{531} - \rho_{570}}{\rho_{531} + \rho_{570}} \quad (1)$$

where ρ_{531} and ρ_{570} is the reflectance at 531 and 570 nm, respectively (Gamon et al., 1993). The relationship between ε and PRI has been proven over a wide range of species plant functional types, and nutrient levels (Peñuelas et al., 1995; Peñuelas et al., 1997a,b; Sims & Gamon 2002), but generalization to satellite observable scales remains difficult. In particular, PRI reflectance is affected by numerous other factors such as the sun-view geometry, soil background reflectance, leaf angle distribution, leaf area, canopy structure and pigment pool size (Asner, 1998; Barton & North 2001; Chen et al., 2003; Drolet et al., 2005; Hall et al., 2008; Hilker et al., 2008b; Strahler & Jupp 1990).

Only a few studies exist that use satellite-based estimates of PRI (Rahman et al., 2004; Drolet et al., 2005; Drolet et al., 2008; Garbulsky et al., 2008) and so far, research has focused on data acquired by the MODerate Resolution Imaging Spectroradiometer (MODIS). Although MODIS lacks a reference band at 570 nm, and Band 11 (531 nm) operates at a fairly coarse spatial resolution of 1 km^2, its daily global coverage and its high geolocation accuracy make it an appropriate choice for exploring the PRI: ε relationship from space (Drolet et al., 2008). Drolet et al., (2005) and Drolet et al. (2008) compared MODIS spectral reflectance to tower-based eddy covariance (EC) measurements acquired at boreal forest sites in Canada. While a significant relationship existed between MODIS observations and EC-measured ε, the work identified a number of key issues (Drolet et al., 2005, 2008) to be addressed in future research: for instance, a strong relationship between PRI and ε was found only for backscatter observations, suggesting that directional reflectance and shading effects overlap and confound the observed PRI signal. Changes in the MODIS viewing geometry alter the proportion of sunlit to shaded canopies and, as a result, the relationship between observed reflectance and photosynthetic down-regulation changes with each observation (Hall et al., 2008; Hilker et al., 2008b,c). Additionally, the MODIS footprint changes with the viewing geometry of the sensor from one overpass to the next and is inconsistent with the footprint of the EC system, which depends on meteorological conditions such as wind-speed and wind direction (Chen et al., 2008; Kljun et al., 2004). As a result, a direct comparison between MODIS-observed PRI and EC observed ε is challenging.

In addition to the uncertainties existing at the surface, Drolet et al. (2005) and Drolet et al. (2008) found MODIS-based PRI observations to be strongly affected by atmospheric scattering effects. Most satellite observations are routinely corrected for atmospheric scattering using pixel-based, single-orbit derived models of the radiative transfer of light through the atmosphere. While this technique is widely applied (Vermote & Kotchenova 2008; Vermote et al., 1997) it uses several simplifying approximations about the land surface reflectance properties in order to retrieve aerosol contents and compute surface reflectance from multi-spectral MODIS measurements. Landscape and temporal variability in the validity of these approximations may obscure subtle changes in narrow-band reflectance such as induced by the photosynthetic down-regulation in leaves. Recently, Lyapustin and Wang (2009) developed a new algorithm that does not depend on these approximations but uses time series of MODIS measurements instead in order to make simultaneous retrieval of atmospheric aerosol and surface bidirectional reflectance. As a result, the Multi-Angle Implementation of Atmospheric Correction (MAIAC) algorithm holds promise to overcome some of the simplifying assumptions underlying single-orbit corrections (Lyapustin & Wang, 2009).

In this paper, we propose a new approach for measuring PRI from space. Instead of comparing MODIS PRI to EC-measured ε directly, a tower-mounted, automated, multi-angular spectroradiometer platform (AMSPEC) (Hilker et al., 2008b, 2007) is used to "translate" EC-measured ε into a tower-measured PRI signal first, by establishing a relationship between tower-measured EC-fluxes and AMSPEC-observed PRI. This AMSPEC-derived PRI is then related to spaceborne reflectance observations. The bidirectional reflectance distribution (BRDF) of this tower-measured PRI (Hilker et al., 2008b; Los et al., 2005) is determined for each MODIS overpass and AMSPECs reflectance is adjusted to the sun-observer geometry of MODIS for each overpass. Both MAIAC (Lyapustin & Wang, 2008, 2009) and standard MODIS algorithm, implemented in the 6S code (Vermote et al., 1997) are used to derive atmospherically corrected PRI for the study area, and both datasets are compared to tower-based PRI measurements. Our results show a significantly enhanced relationship between MAIAC-corrected, MODIS-observed PRI and tower measurements when compared to 6S, which persists throughout the observation period and is independent of viewing directions.

2. Background

Satellite observed reflectance depends on two main parameters, aerosol optical thickness (AOT) and surface reflectance (SR). Aerosols enhance the signal of atmospheric backscattering and attenuate the surface directional reflectance signal as a function of path length. Pixel-based, single-orbit algorithms of atmospheric correction produce a single measurement for every pixel characterized by these two unknowns and, as a result, a-priori information is required to solve for the surface reflectance. For example, the standard MODIS surface reflectance algorithm (MOD09), which uses the dark target aerosol retrieval algorithm (Kaufman et al., 1997; Levy et al., 2007), makes a spectral assumption about surface reflectance in order to evaluate AOT. This assumption relates surface reflectance in the visible (blue and red) spectral bands with MODIS band 7 (2.1 μm) reflectance using a prescribed spectral regression coefficient (SRC). A Lambertian surface model is then used for aerosol retrievals and atmospheric correction. Although it simplifies processing, the Lambertian assumption is known to reduce anisotropy of derived surface reflectance with error dependent on view geometry (e.g., Lyapustin, 1999).

Recently, a new generic aerosol-surface retrieval algorithm, MAIAC, has been developed for MODIS (Lyapustin & Wang, 2008, 2009). MAIAC simultaneously retrieves AOT, SRC and surface BRDF using the time series of MODIS measurements. MAIAC starts with accumulating 3 to 16 days of calibrated and geolocated level 1B (L1B) MODIS data, which are gridded to 1 km resolution. The multi-day data provide different view angles, which are required for the surface BRDF retrieval. Besides, accumulation of a multi-day dataset for a fixed area of 25×25 km^2 creates the number of measurements which exceeds the number of unknowns including AOT and parameters of the BRDF model, so the system of equations can be resolved. The algorithm makes verifiable

assumptions that 1) the surface reflectance changes little during accumulation period, and 2) far from sources, AOT remains relatively constant at short distances (~25 km), because aerosols have a mesoscale range of global variability of ~60–100 km (Anderson et al., 2003). MAIAC is based on a rigorous radiative transfer model (Lyapustin & Knyazikhin, 2001; Lyapustin & Wang, 2005) fully coupled with the Li-Sparse Ross-Thick (LSRT) model of surface BRDF (Wanner et al., 1995).

MAIAC uses a new Cloud Mask algorithm (Lyapustin et al., 2008) which takes advantage of the time series processing. For example, it relies on the fact that consecutive images in cloud-free conditions have a highly reproducible spatial structure, which can be identified by a high covariance between images. Clouds usually randomly disturb this pattern reducing covariance. By keeping a history of the previous surface state, MAIAC also builds a dynamic land–water–snow classification and a surface change mask which allows the algorithm to flexibly choose processing path over different surfaces. MAIAC has a following standard set of gridded products at 1 km resolution from MODIS: column water vapor, cloud mask, aerosol optical thickness and a fraction of fine aerosol mode, as well as parameters of LSRT model, bidirectional reflectance factor (or surface reflectance for a give sun-view geometry), and surface albedo in 12 MODIS bands.

3. Methods

3.1. Study site

The study area is a Canadian Carbon Program (CCP) flux tower site on Vancouver Island, British Columbia, Canada, located at 300 m above sea level (49°52′7.8″ N, 125°20′6.3″ W). The 60-year old second-growth coniferous forest consists of 80% Douglas fir (*Pseudotsuga menziesii* var *menziesii* (Mirb.) Franco), 17% western red cedar (*Thuja plicata* Donn ex D. Don) and 3% western hemlock (*Tsuga heterophylla* (Raf.) Sarg.) and is highly productive with rotation cycles as short as 60 years (Morgenstern et al., 2004). The site is located within the dry maritime Coastal Western Hemlock bio-geoclimatic subzone (CWHxm), which is characterized by cool summers and mild winters with occasional drought during late summer (Humphreys et al., 2006). The stand density is 1100 stems ha^{-1}, with tree height ranging between 30 and 35 m, with an average diameter at breast height (DBH) of 29 cm, while the effective leaf area index (L_e) was estimated to be 7.3 $m^2\ m^{-2}$ using TRAC-LAI-2000 measurements (Chen et al., 2006).

3.2. Tower-based measurements

Continuous, half-hourly fluxes of CO_2 have been measured at the sites since 1997 using an EC system. Net ecosystem exchange (NEE) was determined as the sum of the half-hourly fluxes of CO_2 and the rate of change in CO_2 storage in the air column between ground and EC measurement level (42 m), using a three-axis sonic anemometer–thermometer (model R3, Gill Instruments Ltd., Lymington, UK) and a closed-path CO_2/H_2O infrared gas analyzer (model LI-6262, LI-COR Inc., Lincoln, NE, USA) (Humphreys et al., 2006; Jassal et al., 2007). Incident and reflected PAR [μmol $m^{-2}\ s^{-1}$] was measured from up and downward looking quantum sensors (model 190 SZ, LI-COR Inc.) above and below the canopy and ε was determined from NEE, daytime ecosystem respiration, f_{PAR} (Chen, 1996) and PAR (Humphreys et al., 2006). For details on the method for calculating ε, see (Schwalm et al., 2006).

Canopy spectra were obtained from AMSPEC, an automated tower-based, multi-angular spectroradiometer platform (Hilker et al., 2008b; Hilker et al., 2007) installed at 10 m above the canopy (Fig. 1). This instrument features a motor-driven probe rotating in 11.5° intervals every 30 s, thereby allowing spectrally contiguous observations between 350 and 1200 nm wavelength (bandwidth 3 nm) in a 330° view area around the tower every 15 min. Canopy spectra were obtained from simultaneous measurements of solar irradiance and radiance, sampled every 5 s from sunrise to sunset with the downward looking probe pointing at a vertical zenith angle of 62° (Chen and Black 1991). AMSPEC acquires data within a radius of about 31 m around the tower. Previous research (Chen et al., 2009, Hilker et al., 2008a) based on a footprint model of Chen et al. (2008, 2009) has shown that this area corresponds to about 80% of the average daytime flux-footprint at this site (the prevailing wind direction is south-west). A complete description of the instrument can be found in Hilker et al. (2007). Coinciding with the EC observations, reflectance measurements used for this analysis were collected between April 1st 2006 and September

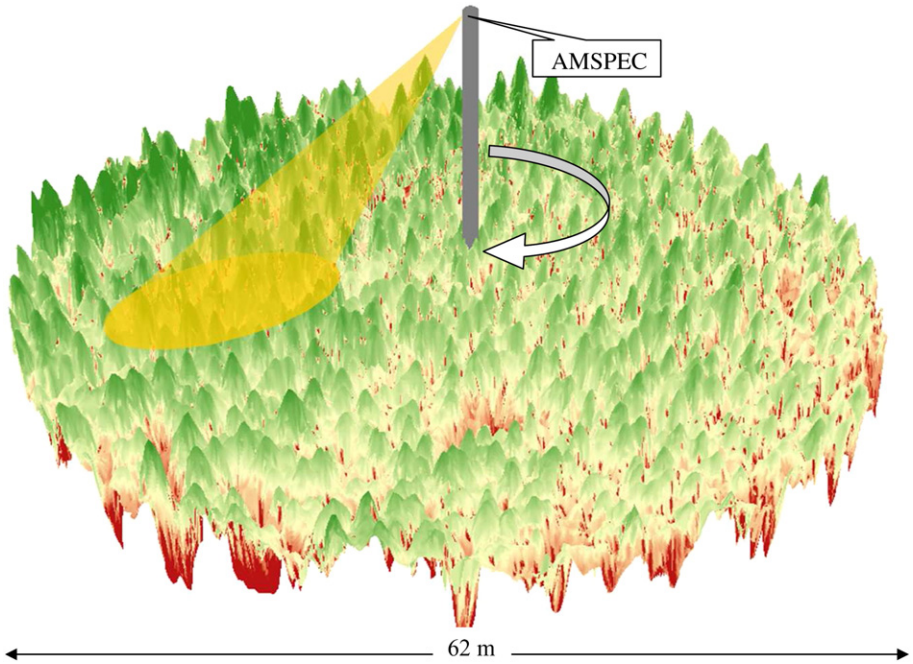

Fig. 1. AMSPEC radiometer system installed at the top of the DF-49 flux tower. The system measures canopy reflectance at a vertical zenith angle of 62°, thereby completing a full rotation every 15 min. Figure adapted from Hall et al. (2008).

15th 2006 during each MODIS overpass (±15 min from peak elevation of the satellite). Clear-day MODIS overpasses were identified by using AMSPEC's measured solar irradiance and comparing it to modeled clear-sky photosynthetically active irradiance (Hilker et al., 2009).

3.3. MODIS data acquisition and atmospheric correction

MODIS observes a given land surface at different viewing geometries during each overpass and, as a result, the MODIS footprint varies in size and location. Observations taken close to nadir will typically produce a relatively small footprint, whereas off nadir data will have larger pixel sizes. Several MODIS standard products, such as the land surface reflectance (MOD09), are "gridded" to a 1 km resolution for use in land process models and applications, thereby including weighted reflectance information of up to multiple adjacent MODIS pixels (Wolfe et al., 1998). Gridding, defined as allocation of geolocated image observations into an output image grid (Wolfe et al., 1998), uses a series of forward and inverse mapping computational steps to convert the observed, distorted input pixels into a regular global raster (Wolfe et al., 1998, Fig. 2). While this method greatly simplifies data handling, it could potentially introduce additional uncertainties to the PRI reflectance, especially in heterogeneous landscapes, as the spatial origin of a reflectance measurement becomes less well defined (Tan et al., 2006). One objective of this study was to investigate the impact of data gridding on the usefulness of MODIS PRI. Consequently, MODIS observations were processed in four different ways, as gridded and non-gridded (swath) datasets using 6S and MAIAC atmospheric correction.

Daily level 1B (L1B) at-sensor radiances (Collection 5) were acquired from the Land Processes Distributed Active Archive Center (LPDAAC) (data portal: https://lpdaac.usgs.gov) for the Terra spacecraft for all clear days during the study period. The top of atmosphere (TOA) radiances for MODIS band 11 (531 nm) and MODIS band 12 (551 nm), were extracted from the hdf data file and converted to TOA reflectances. In a first analysis, MODIS data were gridded to a 1 km resolution using the MODIS reprojection tool and a nearest-neighbor approach. These gridded data were then atmospherically corrected using the 6S algorithm (version 3) (Vermote et al., 1997), based on concomitant aerosol optical thickness obtained from the MODIS aerosol product at 10 km spatial resolution (MOD04) (Drolet et al., 2008). Secondly, 50×50 km^2 gridded subsets of MODIS L1B data for the study period were atmospherically corrected using MAIAC. The MAIAC automatic run generated cloud mask, water vapor, aerosol parameters, spectral surface BRDF and Albedo in 13 MODIS bands, including band 11 and 12 in a 1 km gridded format. In a third and fourth analysis, we then assessed the difference between gridded MODIS observations and non-gridded, swath data. In the case of the 6S corrected dataset, the atmospheric correction was applied to the swath observations directly; in case of MAIAC, swath correction of MODIS pixel encompassing the flux tower (i.e. the tower pixel) was based on the nearest-neighbor aerosol parameters and spectral BRDF shape information from the gridded retrievals.

Table 1
PRI bandwidth and central wavebands as defined by Drolet et al. (2005).

Name	Bandwidth (nm)	Central wavelength (nm)
PRI_{10}	483–493 (Band 10), 526–536 (Band 11)	486.9 (Band 10), 529.6 (Band 11)
PRI_{12}	546–556 (Band 12), 526–536 (Band 11)	546.8 (Band 12), 529.6 (Band 11)
PRI_{13}	662–672 (Band 13), 526–536 (Band 11)	665.5 (Band 13), 529.6 (Band 11)

3.4. Using MODIS wavebands to sense photosynthetic efficiency

Drolet et al. (2005, 2008) tested a number of different MODIS bands as surrogates for the missing PRI band at 570 nm using MODIS band 11 as detection, and MODIS bands 10 (PRI_{10}) 12 (PRI_{12}) or 13 (PRI_{13}) as reference bands (Table 1). While previous results have shown a strong relationship between AMSPEC-derived, stand-level PRI measurements and EC-measured ε throughout the year (Hall et al., 2008; Hilker et al., 2008b), the potential of any of these MODIS-like PRI substitutes to assess photosynthetic down-regulation was unknown for this site. In order to be able to specify an optimal MODIS compatible PRI for the study site, year-round, 3 nm reflectance bands from AMSPEC were downsampled to simulate the 10 nm resolution of the MODIS PRI bands by using the arithmetic mean of the corresponding spectroradiometer wavelengths. AMSPEC-derived PRI_{10}, PRI_{12} and PRI_{13} were then defined as (Drolet et al., 2005),

$$PRI_{ref} = \frac{\rho_{11} - \rho_{ref}}{\rho_{11} + \rho_{ref}} \quad (2)$$

where ρ_{11} is the reflectance of the AMSPEC-simulated MODIS band 11 and ρ_{ref} is the reflectance of any of the AMSPEC-simulated reference bands (10, 12 or 13). PRI_{10}, PRI_{12} and PRI_{13} were compared to EC-measured ε by modeling their BRDF (Hilker et al., 2008b). Hilker et al. (2008b) showed that PRI reflectance observed by AMSPEC is a function of the sun-view geometry, of the sky conditions at the time of measurement and of the physiological status of the vegetation canopy observed (i.e., ε). In order to allow a comparison between the spectrally-derived data and EC measurements, the physiological signal contained

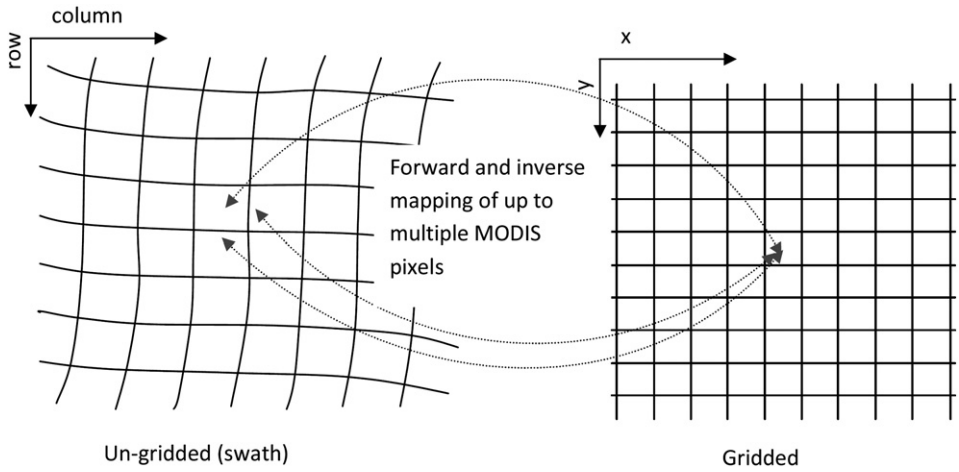

Fig. 2. Illustration of the gridding process undertaken for MODIS products. Depending on size and location of the swath pixel, up to multiple pixels can be contained in a standardized, gridded output pixel. The figure has been adapted from Wolfe et al. (1998).

in PRI_{10}, PRI_{12} and PRI_{13} was extracted from year-round multi-angular AMSPEC observations. Radiometer data were stratified into homogeneous subsets of observations with respect to both sky conditions and tower-measured ε and BRDF models were subsequently fitted to each stratum of each index (PRI_{10}, PRI_{12} and PRI_{13}) (Hilker et al., 2008b). The resulting bidirectional reflectance distribution functions were then used to decompose PRI_{10}, PRI_{12} and PRI_{13} into their sunlit and shaded endmember components (Li & Strahler, 1985, Hall et al., 1995) and related to EC-measured ε (Hilker et al., 2008a).

3.5. Adjusting AMSPEC viewing geometry to MODIS

A major advantage of comparing satellite PRI observations to tower-measured PRI, rather than to EC measurements directly is the possibility to adjust the differences in viewing geometry between the two sensors for each individual satellite overpass, thereby "translating" the EC measurement into a PRI signal. While retrieval of an accurate BRDF for PRI reflectance is difficult from MODIS due to the potential xanthophyll-induced differences in canopy reflectance between individual overpasses (Hall et al., 2008; Hilker et al., 2008a, b), AMSPEC completes a full near 360° sweep of the forest canopy every 15 min. Provided that there are no changes in stand-level illumination (sky conditions), the factors inducing a photosynthetic down-regulation at the stand-level can be assumed to remain relatively constant during this period and, as a result, the variability of stand-level ε is expected to be small with changes in the xanthophyll cycle occurring mostly as a result of sun flecks and shading lower in the canopy. The impact of these changes on the AMSPEC-measured reflectance, however, is negligible, as the vast majority of the observed signal will originate from the top of the canopy (Hall et al., 1992). As a result, it should be possible to derive accurate BRDF models from AMSPEC-measured, stand-level PRI reflectance for a 15 min period, which can then be used to transform the observed PRI into the sun-observer geometry of the respective MODIS overpass (Hilker et al., 2008b; Los et al., 2005).

In this study, we used a kernel-based approach of (Roujean et al., 1992) to model the BRDF of half-hourly PRI observations from AMSPEC (±15 min from peak elevation of the satellite). Using Roujean's notation, the BRDF of PRI can be expressed as the linear combination of isotropic, geometric and volumetric scattering effects (Hilker et al., 2008b; Los et al., 2005; Wanner et al., 1995):

$$\mathrm{PRI}(\theta_v, \theta_s, \Delta\phi) = k_i + k_g F_g(\theta_v, \theta_s, \Delta\phi) + k_v F_v(\theta_v, \theta_s, \Delta\phi). \quad (3)$$

Here, θ_v, θ_s and $\Delta\phi$ are the view zenith, solar zenith and relative azimuth angles; k_i, k_g and k_v are the isotropic, geometric and volumetric scattering coefficients, and F_g and F_v are the geometric and volumetric scattering kernel functions, respectively. These kernel functions may vary with the type of canopy they describe. In this study, we used the Li-Sparse (LS) and Ross-Thick (RT) kernels (Wanner et al., 1995), based on a geometric–optical approach (Li & Strahler 1985) and the radiative transfer theory of Ross (1981).

3.6. Testing the potential to observe photosynthetic down-regulation from MODIS

One goal of this study was to determine whether MODIS reflectance measurements can be used to observe the spectral signal associated to photochemical down-regulation in leaves. For instance, an observed relationship existing between AMSPEC-measured and MODIS-observed PRI could potentially be attributed to simple changes in the viewing geometry, rather than to a photochemical signal. Hall et al. (2008) showed that two conditions are required in order to prove that MODIS-observed PRI does indeed reflect light saturation-induced changes in the xanthophyll cycle pigments of leaves: First, multi-angular PRI reflectance has to change as a function of canopy shadow fractions (α_s) and second, the slope of this relationship has to change with changing levels of ε. Hall et al. (2008) used a LiDAR-derived hillshade algorithm of Hilker et al. (2008c) to observe α_s independently of spectral reflectance. Hillshade algorithms can be applied to model clear-

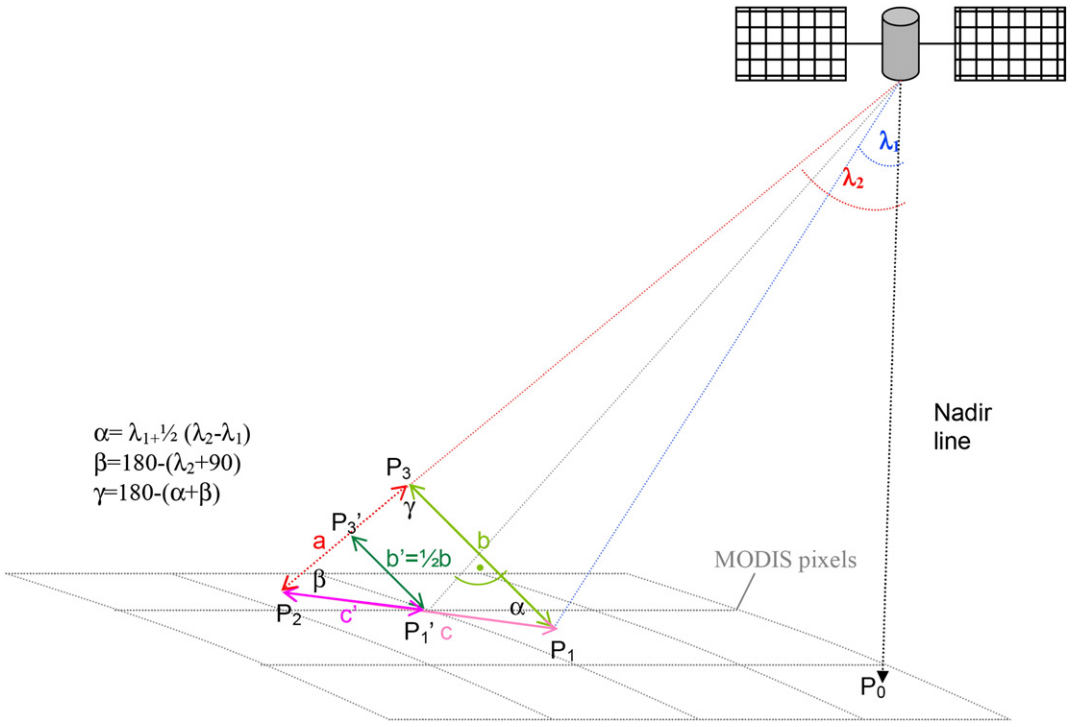

Fig. 3. Deriving the footprint of the MODIS tower pixel from the MODIS geolocation product (MOD03). The corner of the tower pixel is located at half the angular distance between the center pixel and any of its diagonal neighbors. The angle α between P_1' and P_2' can be computed using the view zenith angles λ_1 and λ_2, β is located in the (approximately) rectangular triangle between P_0, P_2 and observing satellite.

Table 2
LiDAR acquisition parameters (adapted from (Hilker et al., 2008a).

Parameter	Performance
Sensor	Mark II (mounted on helicopter)
Laser scan frequency	25 Hz
Laser impulse frequency	40000 Hz
Laser power	<4 W
Maximum scan angle	<20°
Type of scanning mirror	Oscillating
Laser beam divergence	<0.5 mrad
Measurement density	0.5–0.8 hits per sq m^{-2}
Flight altitude above ground	900 m
Flight speed	25–30 m s^{-1}

sky canopy shadowing for a given sun position and are commonly used in three-dimensional mapping (Pellegrini et al., 2003; Van Den Eeckhaut et al., 2005). For details on deriving α_s from hillshades, see Hilker et al. (2008c). Hillshade algorithms can potentially also be used for space-borne observations if the extent and location of the MODIS pixel encompassing the flux tower (i.e. tower pixel) is known. The footprint of the MODIS swath data varies with the viewing geometry for each overpass, and as a result, the bounding coordinates of the tower pixel need to be inferred for each MODIS acquisition individually. The extent of MODIS swath data can be determined using the MODIS geolocation product (MOD03), describing the center location (latitude and longitude) and the sensor and sun zenith and azimuth angles for each pixel within a scene (Fig. 3). The four corners of the tower pixel can be approximated using half the angular distance (b) between the center of the tower pixel and the center of each of its diagonal neighbors. This approximation is valid when the curvature of the Earth is neglected, which is reasonable for the expected pixel size (see Fig. 3).

The MOD03 product was downloaded from the EOS-data portal coincident with the MOD02 level 1B data. Airborne LiDAR data for the study area were acquired on 8 June 2004 with a spacing density of 0.7 hits m^{-2} and a spot size of 0.19 m (for system details see Table 2). Separation between vegetation and terrain was carried out by iteratively classifying LiDAR data into either ground or non-ground returns (Terrascan v. 4.006, Terrasolid, Helsinki, Finland). The canopy was described using a canopy surface model (CSM), one of which was generated for each overpass from non-ground returns. α_s was approximated by hillshading each CSM using the sun geometry at the time of the MODIS observation and intersecting it with the respective observer geometry of the satellite (Hilker et al., 2008c).

In order to investigate the sensitivity of MODIS PRI to α_s, MODIS data were stratified with respect to ε (Hilker et al., 2008b) and the relationship between MODIS PRI and α_s was investigated for each stratum. ε was calculated from averaged half hour flux observations around each MODIS overpass (satellite peak ± 15 min) and strata boundaries were defined based on previous findings ($0<\varepsilon\leq 0.2$ g C MJ^{-1}, $0.2<\varepsilon\leq 0.4$ g C MJ^{-1} and $0.4<\varepsilon\leq 0.6$ g C MJ^{-1}) (Hilker et al., 2008b). Stratified clear-sky PRI should vary only as a function of α_s as the more sun-exposed leaves should show a stronger light-saturated signal than shaded leaves, especially under situations where photosynthesis is limited by factors other than light (Hall et al., 2008; Hilker et al., 2008b).

4. Results

4.1. Optimal MODIS wavebands for measuring photosynthetic efficiency

Fig. 4 shows the relationship between BRDF adjusted, AMSPEC-derived PRI (Fig. 4A), PRI_{10} (Fig. 4B), PRI_{12} (Fig. 3C) and PRI_{13} (Fig. 4D) and EC-measured ε, respectively (daily means). PRI reflectance adjusted to the hotspot (= 100% sunlit canopy) and darkspot (= 100% shaded canopy) (Hilker et al., 2008a) is shown for each index to

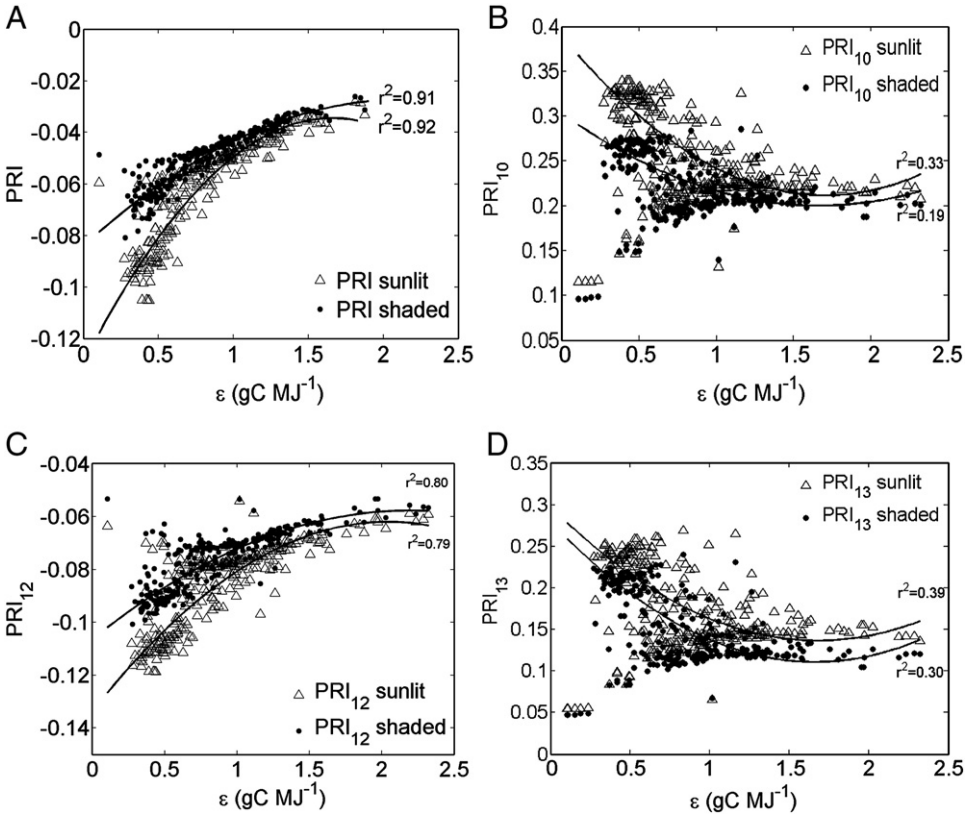

Fig. 4. A–D: Relationship between daily PRI (A), PRI_{10} (B) PRI_{12} (C) and PRI_{13} (D) and daily EC-determined ε, respectively throughout the study period. Fig. 4A shows the PRI using 570 nm as reference band (Gamon et al., 1993), PRI_{10}, PRI_{12}, and PRI_{13} follow the definition given by Drolet et al., 2005. The use of MODIS bands instead of the reference wavebands proposed by Gamon et al., 1993) weakens the relationship between the optical signal and ε (Hilker et al., 2008a); however, PRI_{12} still yields a strong correlation to ε and, as a result, Band 12 was selected as the best substitute for the missing reference band at 570 nm.

illustrate the dependency on shadow fractions. For the relationships presented in Fig. 4A and C, the PRI values measured at the darkspot were higher than those measured at the hotspot, indicating higher levels of ε in shaded canopies. Also, the difference between hotspot and darkspot reflectance increased with decreasing levels of ε. For the negative relationships shown in Fig. 4B and 3D, this pattern is reversed. The range of PRI values shown in Fig. 4A and C is similar, whereas PRI_{10} and PRI_{13} yield positive index values. While the PRI proposed by Gamon et al. (1992), Gamon et al. (1993) shows the strongest relationship to EC-measured ε, it is only presented here as a reference (Hilker et al., 2008a), since MODIS lacks a corresponding reference band at 570 nm. Out of the three remaining MODIS reflectance indices proposed by Drolet et al., (2008), PRI_{12} yields the strongest relationship to EC-measured ε ($r^2=0.80$ and $r^2=0.79$ for hotspot and darkspot, respectively, $p<0.01$). PRI_{10} and PRI_{13} show only weak to moderate relationships to EC-measured ε ($0.19\leq r^2\leq 0.39$; $p<0.05$) and were excluded from subsequent analysis.

4.2. Comparison between MODIS-observed PRI and AMSPEC-observed PRI

Fig. 5 illustrates the result of the MAIAC correction of MODIS data acquired for the study area. The figure shows the MODIS TERRA top of atmosphere (TOA) reflectance for the red, green and blue (RGB) bands, the MAIAC-derived cloud mask, a RGB-normalized BRDF, the surface reflectance, SRC with scale 0–1 shown by color bar and retrieved AOT at a scale 0–0.6 for 2 periods of 9 consecutive MODIS TERRA observations. The reflectance scale for the RGB images is 0–0.15. The lower-left corner is a mountainous area covered by snow, which may persist throughout the summer.

Fig. 6 shows an overview of the range in θ_v and $\Delta\phi$ for the MODIS observations acquired during the study period. The view zenith angles (Fig. 6A) varied between 30° and 70°, $\Delta\phi$ ranged between 130° and 150° for the observations closer to the forward scattering direction, and between 20° and 50° for the measurements closer to the backscattering direction. During the same period, AMSPEC scanned the canopy at the full range of relative azimuth angles and at a constant $\theta_v=62°$. The coefficients of determination for the BRDF models fitted to AMSPEC PRI_{12} observations at the times of MODIS overpasses under clear-sky conditions ranged between 0.80 and 0.99 ($p<0.01$).

Fig. 7 shows the relationship between 6S-corrected MODIS PRI_{12} and directionally-adjusted AMSPEC PRI_{12} measurements throughout the study period. Results using the gridded MODIS data are presented in Fig. 7A, Fig. 7B shows the relationship between AMSPEC-observed PRI_{12} and MODIS swath data. MODIS observations include measurements of both the forward and backscattering directions. The relationship between tower-measured PRI_{12} and 6S-corrected MODIS

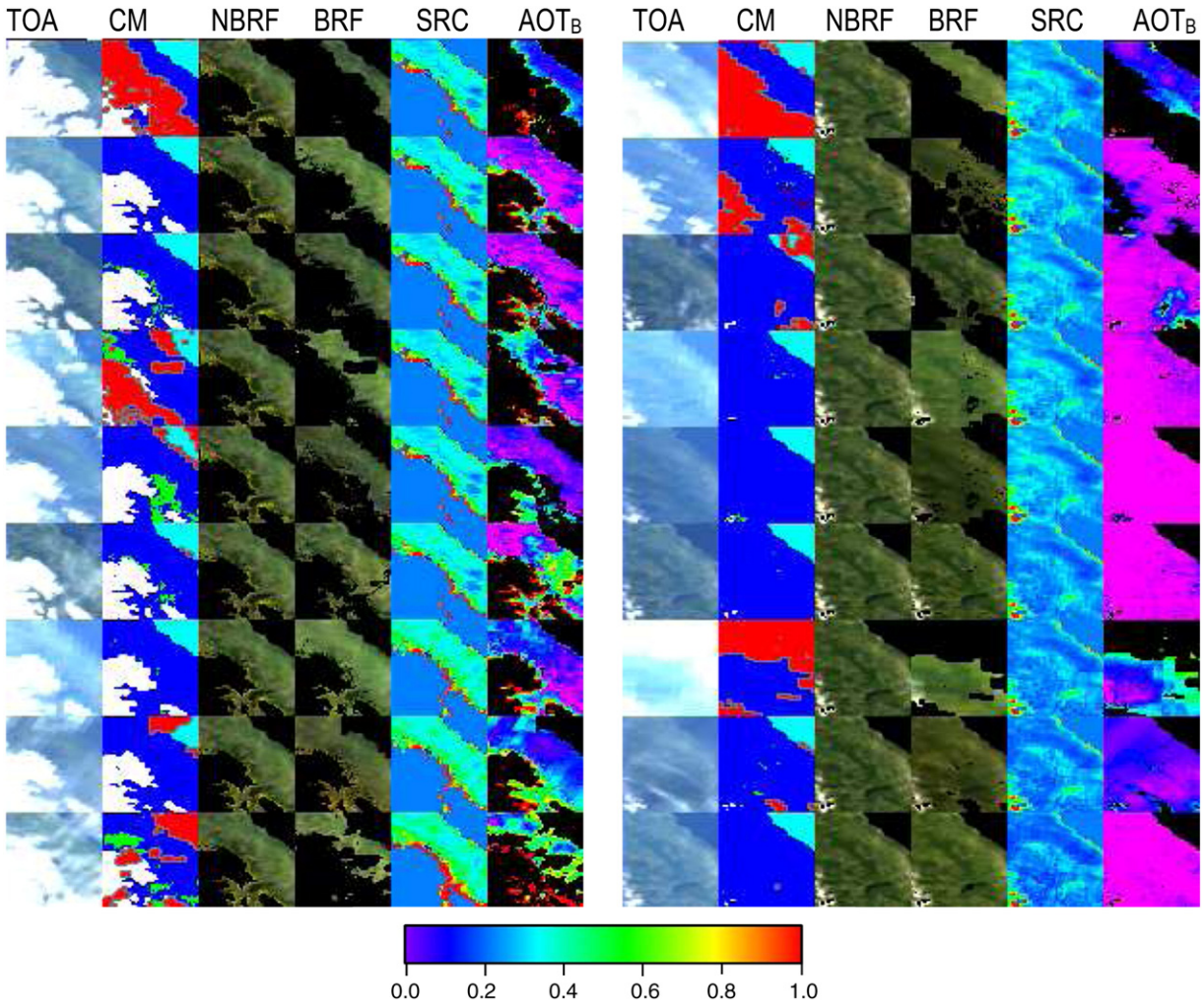

Fig. 5. Illustration of the MAIAC algorithm for the study area (pixel 10, 10). Shown vertically are 9 consecutive images for two periods, May 25–31, and September 20–25 of 2006. Columns have the following correspondence (scale): 1 — MODIS TERRA TOA RGB, 2 — cloud mask, 3 — RGB Normalized BRDF (computed using retrieved LSRT parameters for fixed view geometry of SZA = 45° and nadir view), 4 — RGB BRDF (or surface reflectance), 5 — SRC with scale 0–1 shown by color bar, 6 — retrieved AOT with scale 0–0.6. The cloud mask has the following legend: white, blue and light blue — CLEAR over snow, land and water, respectively; green — possibly clear (AC not performed); red — cloudy. The reflectance scale for RGB images is 0–0.15. The low-left corner is a mountainous area covered by snow, which may persist throughout the summer.

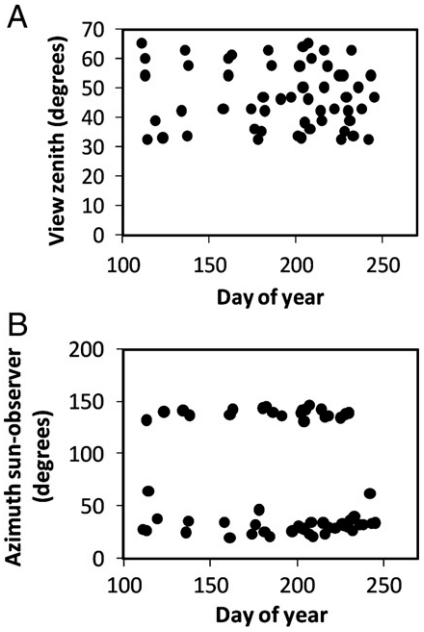

Fig. 6. View zenith angles of MODIS observations acquired during the study period at the DF-49 tower site. The observed view zenith angles varied between 30° and 70°. B: Relative azimuth between sun and observer of all image data acquired during the study period. Data can be separated into back scatter observations (20° to 50°) and forward scatter observations (130° to 150°).

PRI_{12} was insignificant for both gridded and swath observations when including all viewing directions (Fig. 7A, B). Tower-measured and MODIS-observed PRI_{12} did reveal an improved and somewhat significant correlation when considering only observations closer to the backward-scatter direction (Fig. 7C and D), This was however, still relatively weak for both gridded and swath data and especially in the case of the swath data, deviated significantly from the 1:1 line. This result agrees with previously reported (Drolet et al., 2008).

Fig. 8 shows the relationship between tower-measured AMSPEC PRI_{12} and MAIAC-corrected MODIS PRI_{12}. Fig. 8A presents data for the gridded case, Fig. 8B shows MAIAC-corrected MODIS swath data. Both figures showed a strong linear relationship to tower-measured PRI. The coefficient of determination was 0.58 for the gridded data and 0.74 for the swath data, respectively ($p<0.01$). Importantly, both datasets include observations close to the forward and backscatter observations. The MAIAC-corrected MODIS PRI_{12} overestimated the AMSPEC-derived PRI_{12} slightly, however, this bias was relatively consistent, especially in the case of the swath data and a high level of precision was maintained.

4.3. Observing photosynthetic down-regulation from MODIS

The result of the footprint calculation for the MODIS swath data is shown in Fig. 9; for illustration purposes only two examples are presented, for days of year (DOY) 249 and 220. At DOY 249, observations were made at a view zenith angle closer to nadir ($\theta_v = 33.85°$, $\theta_s = 49.32°$ and $\Delta\phi = 41.5°$) and, as a result, the MODIS footprint is relatively small. The tower pixel observed on DOY 249 encompassed an area of ~1,073,000 m^2. On DOY 220, MODIS-observed the study site at a far-off nadir look angle ($\theta_v = 57.34°$, $\theta_s = 41.87°$ and $\Delta\phi = 29.7°$), and, as a result, the tower pixel encompassed a much larger area (~2,937, 100 m^2), which also included some non-forested patches. Fig. 10 shows the LiDAR-derived CSM for the footprint observed at DOY 249. The observation area of AMSPEC was constant throughout the study period and is superimposed on the 3D-model. The proportion of a MODIS pixel covered by AMSPEC varied with MODIS viewing geometry and ranged between 0.1 and 0.4%. The LiDAR estimated shadow fraction for the pixel shown in Fig. 10 was 40% at the time of observation. Overall, α_s varied between 37% and 68% depending on the

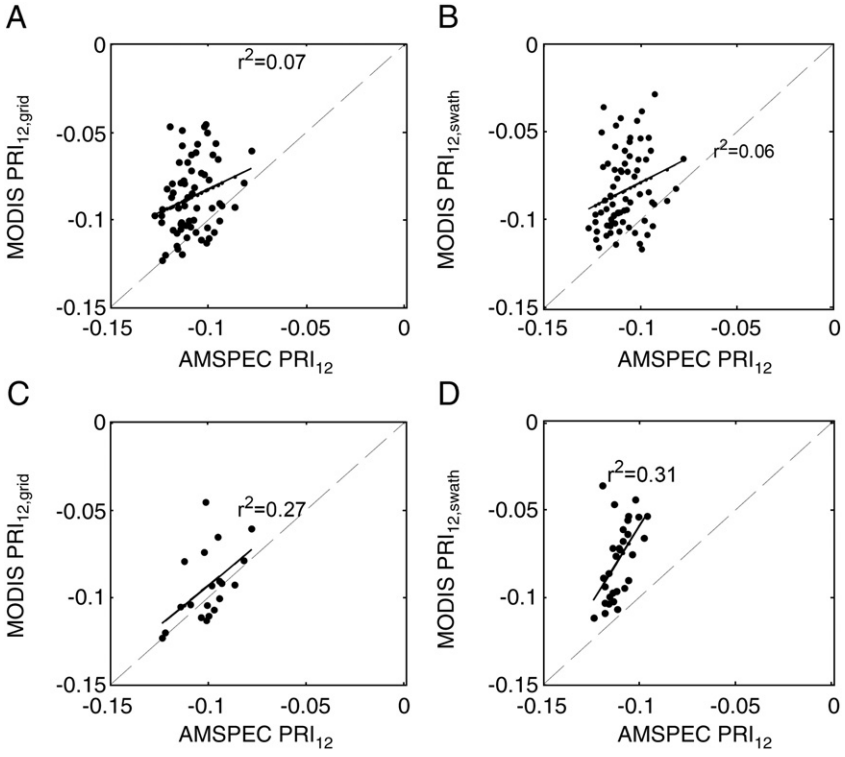

Fig. 7. Relationship between 6S-corrected MODIS PRI_{12} and directionally-adjusted AMSPEC PRI_{12}. The dashed line represents the 1:1 line. Figs. 7A and 7B show data derived under all view angles for gridded and non-gridded swath data, respectively. Note that the gridded 6S corrected data yield a positive PRI_{12} (Drolet et al., 2005). Figs. 7C and D represent 6S corrected MODIS observations for only the backscatter data. The relationship to AMSPEC-observed $PRI1_{12}$ is improved but still relatively weak.

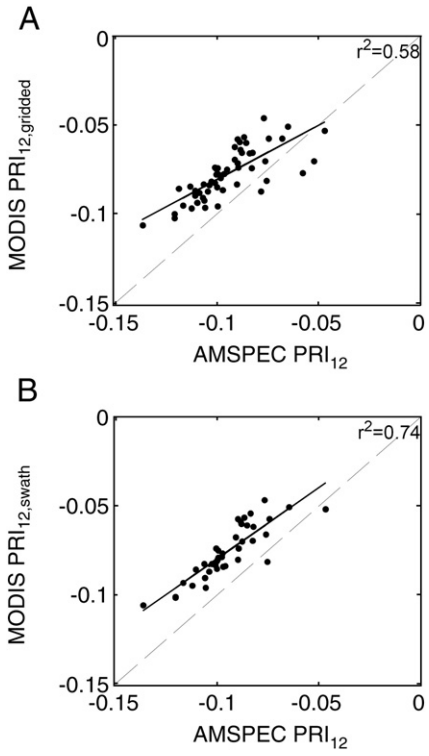

Fig. 8. Relationship between MAIAC-corrected MODIS PRI_{12} and directionally-adjusted AMSPEC PRI_{12}. The dashed line represents the 1:1 line. Fig. 8A and 6B show MODIS observations derived at all view angles for gridded and non-gridded swath data, respectively. The relationship is significantly enhanced over the use of single-orbit derived atmospheric correction.

MODIS viewing geometry and solar position. The reflectance of MAIAC-corrected, MODIS-observed ρ_{11} and ρ_{12} was strongly linearly related to LiDAR-derived shadow fractions (Fig. 11). The coefficients of determination were $r^2=0.69$ and $r^2=0.73$ for ρ_{11} and ρ_{12}, respectively ($p<0.01$). The sensitivity of both bands to α_s was, however, different as the slope of ρ_{11} was smaller than that of ρ_{12} (Fig. 11).

The relationship between MODIS PRI_{12} and canopy shadow fractions for the three different ε-strata is presented in Fig. 12A–C. Fig. 12A includes all observations made under conditions where $0.0<\varepsilon<0.2$ g C MJ^{-1}, Fig. 12B shows MODIS data observed under $0.2<\varepsilon<0.4$ g C MJ^{-1} and Fig. 12C contains all observations acquired with $0.4<\varepsilon<0.6$ g C MJ^{-1}. In all three cases, a significant relationship exists between PRI_{12} and canopy shadow fractions, with the highest coefficient of determination found for the highest light use efficiencies (Fig. 11C). PRI values were, on average, smallest for the lowest ε values ($\varepsilon<0.2$ g C MJ^{-1}) and largest for the least photosynthetically restrained canopy presented in Fig. 12C. Importantly, the slope of the relationship between PRI_{12} and α_s is smallest where ε is highest, indicating that the photosynthetic activity of the sunlit part of the canopy was comparatively higher under situations where the photosynthetic reaction was limited by light (for instance compared to Fig. 12B). Largest differences between sunlit and shaded canopies were found in the intermediate case with photosynthesis still active but reduced due to increased light levels.

5. Discussion and conclusions

This study introduced a new approach for measuring photosynthetic light use efficiency from MODIS using the MAIAC algorithm. A tower-mounted, multi-angular spectroradiometer platform (AMSPEC) (Hilker et al., 2008b, 2007) was used to upscale ground measurements to space by translating the EC-measured flux data into an optical, MODIS compatible signal. Importantly, the AMSPEC-derived model of the BRDF allowed us to account for differences in the observation geometry and helped to reduce uncertainties related to the discrepancies between the MODIS footprint and that of the EC system. Out of the originally proposed vegetation indices used to observe ε from MODIS (Drolet et al., 2005), PRI_{12} showed the best relationship to EC-measured ε (Fig. 4). This result using the MODIS band centered 546.9 nm as a reference, is consistent with the findings of Gamon et al. (1992), who reported that the optimal wavelength for correlating stand-level PRI to ε was actually 551 nm, rather than 570 nm, as the band at 551 nm was found to better normalize the reflectance for variations in vegetation greenness. While the AMSPEC measurements still yielded a better relationship between PRI and ε when using 570 nm as a reference band, the MODIS footprint was much larger than that of AMSPEC, and as a result, further research may be required to establish an optimal reference band when observing larger areas.

As opposed to Drolet et al. (2008), only weak relationships were found for between ε and PRI_{10} and ε and PRI_{13}. Further investigations may help to clarify the reasons for this discrepancy; one possible explanation could be that the relationship between PRI_{10} and ε, and PRI_{13} and ε may be species-dependent. Additionally, PRI_{10} and PRI_{13} may also be more sensitive to noise at larger view zenith angles ($\theta_v=62°$), due to increased variability in pixel content as θ_v increases.

The results shown in Fig. 7 confirm the previously described dependency of 6S-corrected MODIS observations on $\Delta\phi$ (Drolet et al., 2005, 2008). Only PRI derived from MODIS observations closer to the backscatter direction yielded a significant relationship to AMSPEC-observed PRI (Drolet et al., 2005). This and an overall lack of correlation between AMSPEC PRI and 6S-corrected MODIS data is indicative of incomplete compensation of atmospheric distortions for these two narrow wavebands. A novel conclusion to be drawn from this study is that the dependency of 6S-corrected PRI_{12} on $\Delta\phi$ can be largely attributed to atmospheric scattering effects (Fig. 7C and D), as 1) this study accounted for differences in bidirectional reflectance distribution using AMSPEC observations and 2) MAIAC-corrected MODIS observations did not show this distinction between forward and backward-scatter observations. The restriction on the use of backscatter observations would limit the applicability of spaceborne PRI observations over larger areas as a range of view angles is essential for isolating the physiological signal of PRI measurements from other effects (Hall et al., 2008; Hilker et al., 2008b). The results of this study suggest that the multi-angle approach implemented in MAIAC may be better suited for detecting subtle changes in narrow waveband reflectance such as induced by PRI.

Two main differences between current implementation of 6S and the MAIAC AC algorithm can be identified: 1) 6S was used with ancillary aerosol input from MODIS aerosol algorithm (MOD04), whereas MAIAC makes internal aerosol retrievals. This way was adopted for 6S because current MODIS surface reflectance algorithm (MOD09) does not make an operational atmospheric correction of the "ocean" bands B11 and B12. Use of ancillary rather internally retrieved aerosol data may have affected the 6S results. We expect this error source to be small because according to MAIAC and MOD04 AOT, the atmosphere was very clean during the study period, and because the accuracy of Collection 5 MOD04 product is known to be very high over dark dense vegetation (e.g., Levy et al., 2007) to which category belongs the study area. 2) 6S assumes a Lambertian surface reflectance model, while MAIAC uses a rigorous radiative transfer model coupled with LSRT BRDF model. The use of a Lambertian assumption in 6S is equivalent to re-distribution of surface-reflected light into all directions equally. This assumption may reduce the accuracy of the atmospheric correction in the PRI detection band, as the dependency of this band on shadow fractions is stronger than that of the reference band (Hall et al., 2008, Hilker et al., 2008b).

The use of MAIAC greatly enhanced the relationship between MODIS and AMSPEC reflectance, thereby underlining the importance of atmospheric correction for narrow-band indices such as PRI_{12}. Given

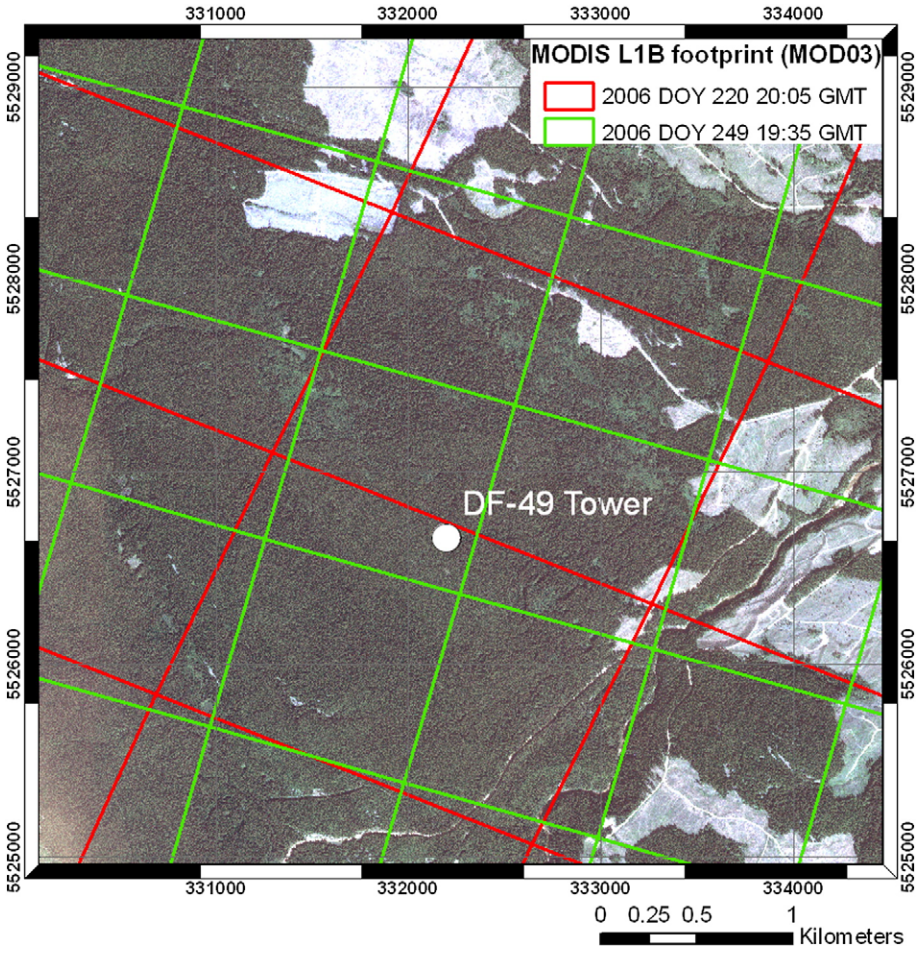

Fig. 9. Quickbird image of the study site with superimposed MODIS swath footprints for the example of DOY 220 and DOY 249, 2006. The footprint of the swath data varies with the sun-observer geometry and, as a result, is different for each overpass. While the forest structure around the tower is relatively homogenous, MODIS observations in far-off nadir direction may include other vegetation types such as harvested areas and were therefore eliminated from this study.

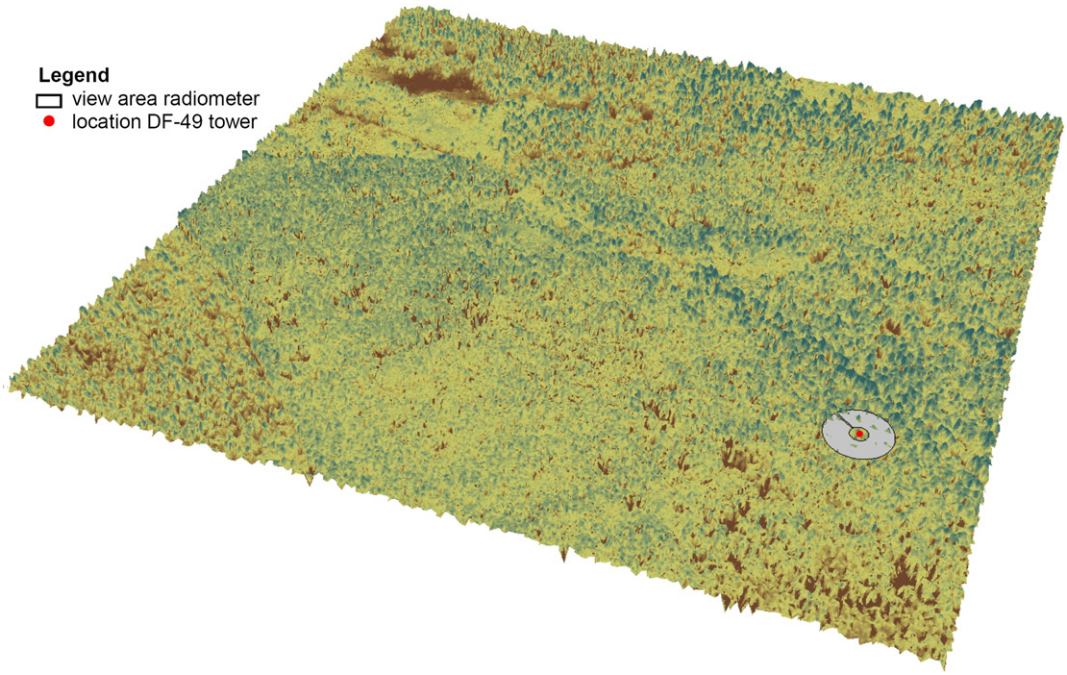

Fig. 10. LiDAR-derived canopy surface model (CSM) of a MODIS pixel for the example of the MOD03 data acquired at DOY 249, 2006. The location of the flux tower is indicated in the lower right corner of the pixel, as is the estimated footprint of AMSPEC (see Hilker et al., 2007 for details). While the forest structure of this pixel is relatively homogenous, far-off nadir observations may include harvested areas as shown in Fig. 8 and were therefore eliminated from this study.

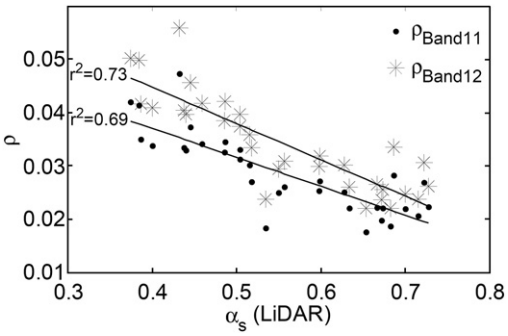

Fig. 11. Relationship between LiDAR-derived shadow fractions and the MAIAC-corrected MODIS-observed PRI bands 11 and 12. The slope of the relationship varies between band 11 and 12. The regression equations are $f(x) = 0.0588–0.0544x$ for Band 11, and $f(x) = 0.0721–0.0682x$ for Band 12, respectively. The figure contains clear-sky observations collected throughout the study period with far-off nadir observations containing non-forested elements excluded (see Fig. 9).

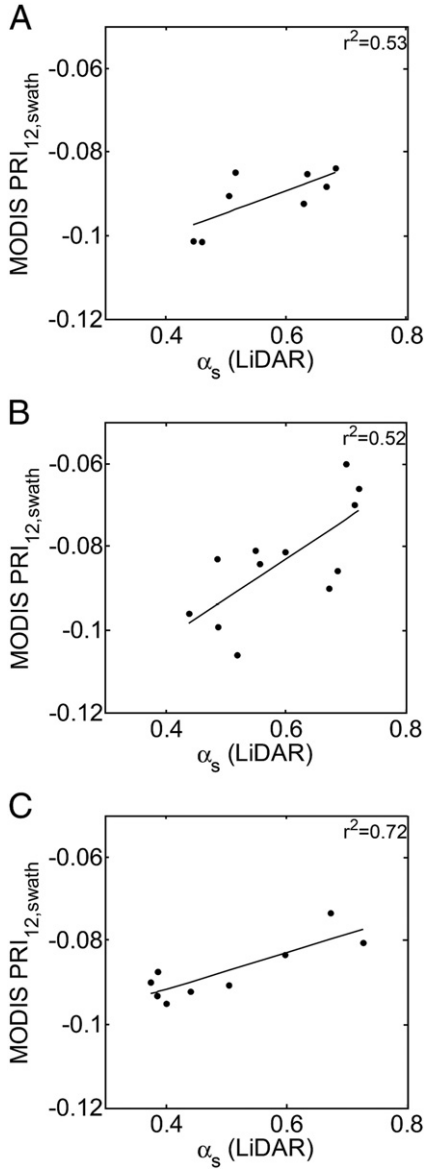

Fig. 12. Relationship between MAIAC-corrected MODIS PRI_{12} derived from non-gridded, swath observations and canopy shadow fractions (α) for three different ε strata, 0.0 g C MJ_{-1} < ε < 0.2 g C MJ_{-1} (Fig. 12A), 0.2 g C MJ_{-1} < ε ≤ 0.4 g C MJ_{-1} (Fig. 12B) and 0.4 g CM_{-1} < ε < 0.6 g C MJ_{-1} (Fig. 12C). All strata show a significant relationship between α_s and PRI_{12}, indicating the sensitivity of PRI_{12} to light saturation-induced photosynthetic down-regulation in leaves. The figure contains clear-sky observations collected throughout the study period with far-off nadir observations containing non-forested elements excluded (see Fig. 9).

very subtle changes in the plant reflectance at 531 nm as a function of photosynthetic down-regulation, heterogeneity of the site and variations of MODIS footprint with view geometry, achievement of high correlation (~0.75) for PRI with ground-based measurements for the full range of viewing geometries can be considered as an initial, though rigorous, validation of the new atmospheric correction algorithm.

MAIAC-corrected swath data yielded a better relationship to AMSPEC PRI_{12} observations than the gridded MODIS PRI_{12} reflectance (Fig. 8A and B). We attribute this to the heterogeneity of the study area with non-forested patches confounding the observed PRI_{12} signal (see Fig. 9). Grid-interpolated reflectance is more likely to include pixel values derived from other, non-forested areas, especially in off nadir viewing direction. Swath data provide a better control over the actual area of observation and pixel with non-forested patches can be eliminated from the analysis. Accurate assessment of the MODIS footprint (Fig. 9) has important implications for the assessment of shadow fractions of a given MODIS pixel. The approach presented in this paper demonstrated a simple method to approximate the pixel extent using the MODIS geolocation product. The LiDAR-derived hillshade algorithm provided an effective means for estimating canopy α_s from remote sensing. The strong linear relationship observed between MODIS ρ_{11}, ρ_{12} and α_s, respectively (Fig. 10) confirmed that shadow fractions have been accurately assessed from LiDAR. This result is also confirmed by previous studies (Hall et al., 2008; Hilker et al., 2008c). It should, however, be noted that hillshade-based modeling of the canopy surface does not include within-crown shading effects and is therefore likely to underestimate canopy shadow fractions (Hilker et al., 2008c). The impact of this restriction on MODIS reflectance, however, is expected to be small due to the coarse spatial resolution of MODIS observation. Another possible limitation for the use of LiDAR to estimate canopy shadow fractions at other sides may be the availability of airborne LiDAR data. It should, however, be possible to substitute these measurements by either relating the overall brightness of broader xanthophyll-insensitive reflectance bands to shadow fractions (Fig. 11) or using LiDAR-derived hillshades to calibrate a geometric–optical models to express α_s (Drolet et al., 2008).

The proportion of the MODIS tower pixel covered by the AMSPEC footprint is relatively small and may therefore fail to adequately represent PRI in areas with a more mixed species or age composition. This problem may be mitigated using spectral measurements from taller towers which will encompass larger footprint areas (Chen et al., 2005). An important result of this study is the finding that MODIS-based PRI_{12} was strongly related to α_s across all the observed ε strata. Similar results have previously been found by Hall et al. (2008) and Hilker et al. (2008b) when comparing BRDF scattering components of PRI reflectance to ε observations. The steepest slope between α_s and MODIS PRI_{12} was found for the intermediate ε class, whereas changes in α_s triggered a less distinct spectral response in the lowest ε stratum ($0.0 \leq \varepsilon \leq 0.2$ g CM J^{-1}). Photosynthesis of data collected for the lowest ε stratum is minimal for both, shaded and sunlit canopies. The difference in PRI_{12} between sunlit and shaded parts of the canopy is then increasing when the trees are starting to photosynthesize, but the performance of this photosynthetic reaction is still limited by factors other than light, especially in the sunlit part of the canopy. The slope between α_s and PRI_{12} once again decreases when favourable environmental conditions allow enhanced levels of photosynthesis in all parts of the canopy (Hilker et al., 2008b). The AMSPEC-observed spectra (Fig. 4) show a similar trend, the largest difference between sunlit and shaded parts is, however, found at the lowest levels of ε (Fig. 4A, Fig. 4C). One possible explanation for this could be the significant difference in the spatial scale observed by MODIS and AMSPEC with the tower-based instrument observing much more distinct difference between shaded and sunlit canopies, further research will be required to address this phenomenon more in detail.

In an operational sense, the translation of the retrieved PRI signal into ε (g C MJ^{-1}) can be a restriction to the method introduced in this

study, as canopy level ε represents an integrated measurement of the bulk canopy, including sunlit and shaded leaves, whereas the model introduced in this work only yields PRI for sunlit and shaded end-members. As a result, additional knowledge of the mean canopy shading will be required throughout the observation period to derive bulk canopy ε from PRI (see Hilker et al., 2008a). Such data may, however, become available in the near future on a global scale from spaceborne LiDAR missions such as DESDynI (Deformation, Ecosystem Structure and Dynamics of Ice).

Tower-based eddy covariance measurements are vital components of current efforts to determine GPP at a global scale. While tower-based measurements provide reliable estimates of carbon exchange at local scales, satellite remote sensing are required for spatially continuous estimates of global carbon fluxes (Heinsch et al., 2006; Running et al., 2004a; Turner et al., 2003). Due to the differences in methodology, a direct comparison between spaceborne observations and EC data will result in measurement uncertainties, such as differences in footprint or viewing geometry. The results presented in this study demonstrated an approach to overcome some of these important issues related to upscaling EC measurements to space. A proposed network of AMSPEC like spectroradiometer instruments based on existing flux towers could greatly advance existing upscaling efforts by helping to calibrate coarser scale observations to tower-based measurements and allowing an adjustment for different vegetation and land-cover types. Approaches like the one presented in this study are therefore vital steps towards the ultimate goal of deriving accurate GPP observations entirely from space.

Acknowledgements

The LiDAR data for this project was acquired by Benoît St-Onge as part of an ongoing collaborative project with funds provided by NSERC and BIOCAP. We would like to thank Zoran Nesic, Dominic Lessard, and Rick Ketler from UBC Faculty of Land and Food Systems (LFS) for their assistance in technical design, installation, and maintenance of the radiometer platform. This research is partially funded by the Canadian Carbon Program, NSERC and BIOCAP. The work of Dr. Lyapustin and Dr. Wang was supported by the NASA Terrestrial Ecology Program (Dr. D. Wickland). The work of Dr. Hall was supported by NASA as part of the "Synergistic study for LiDAR and passive optical remote sensing of forest horizontal structure in support of the DESDYNI mission" (NASA Grant NNXD8AL55G).

References

Anderson, T. L., Charlson, R. J., Winker, D. M., Ogren, J. A., & Holmen, K. (2003). Mesoscale variations of tropospheric aerosols. *Journal of the Atmospheric Sciences*, *60*, 119−136.

Asner, G. (1998). Biophysical and biochemical sources of variability in canopy reflectance. *Remote Sensing of Environment*, *64*.

Asrar, G., Fuchs, M., Kanemasu, E., & Hatfield, J. (1984). Estimating absorbed photosynthetic radiation and leaf area index from spectral reflectance in wheat. *Agronomy Journal*, *76*, 300−306.

Barton, C. V. M., & North, P. R. J. (2001). Remote sensing of canopy light use efficiency using the photochemical reflectance index — Model and sensitivity analysis. *Remote Sensing of Environment*, *78*, 264−273.

Chen, B., Chen, J. M., Mo, G., Black, T. A., & Worthy, D. E. J. (2008). Comparison of regional carbon flux estimates from CO_2 concentration measurements and remote sensing based footprint integration. *Global Biogeochemical Cycles*, *22*, GB2012. doi:10.1029/2007GB003024.

Chen, B. Z., Black, T. A., Coops, N. C., Hilker, T., Trofymow, J. A., & Morgenstern, K. (2009). Assessing tower flux footprint climatology and scaling between remotely sensed and eddy covariance measurements. *Boundary-Layer Meteorology*, *130*, 137−167.

Chen, B. Z., Chen, J. M., & Worthy, D. E. J. (2005). Interannual variability in the atmospheric CO_2 rectification over a boreal forest region. *Journal of Geophysical Research-Atmospheres*, 110.

Chen, J., Rich, P., Gower, S., Norman, J., & Plummer, S. (1997). Leaf area index of boreal forests: Theory, techniques, and measurements. *Journal of Geophysical Research*, *102*, 29 429−429 443.

Chen, J. M. (1996). Canopy architecture and remote sensing of the fraction of photosynthetically active radiation absorbed by boreal conifer forests. *IEEE Transactions on Geoscience and Remote Sensing*, *34*, 1353−1368.

Chen, J. M., & Black, T. A. (1991). Measuring leaf-area index of plant canopies with branch architecture. *Agricultural and Forest Meteorology*, *57*, 1−12.

Chen, J. M., Govind, A., Sonnentag, O., Zhang, Y. Q., Barr, A., & Amiro, B. D. (2006). Leaf area index measurements at Fluxnet-Canada Forest Sites. *Agricultural and Forest Meteorology*, *140*, 257−268.

Chen, J. M., Liu, J., Leblanc, S. G., Lacaze, R., & Roujean, J. L. (2003). Multi-angular optical remote sensing for assessing vegetation structure and carbon absorption. *Remote Sensing of Environment*, *84*, 516−525.

Collelo, G. D., Grivet, C., Sellers, P. J., & Berry, J. A. (1998). Modeling of energy, water, and CO_2 flux in a temperate grassland ecosystem with SiB2: May–October 1987. *Journal of Atmospheric Sciences*, *55*, 1141−1146.

Comins, H. N., & McMurtrie, R. E. (1993). Long-term response of nutrient-limited forests to CO_2 enrichment — Equilibrium behavior of plant–soil models. *Ecological Applications*, *3*, 666−681.

Daughtry, C. S. T., Gallo, K. P., & Bauer, M. E. (1983). Spectral estimates of solar-radiation intercepted by corn canopies. *Agronomy Journal*, *75*, 527−531.

Demmig, Adams, B., & Adams, W. W. (1996). The role of xanthophyll cycle carotenoids in the protection of photosynthesis. *Trends in Plant Science*, *1*, 21−26.

Drolet, G. G., Huemmrich, K. F., Hall, F. G., Middleton, E. M., Black, T. A., Barr, A. G., & Margolis, H. A. (2005). A MODIS-derived photochemical reflectance index to detect inter-annual variations in the photosynthetic light-use efficiency of a boreal deciduous forest. *Remote Sensing of Environment*, *98*, 212−224.

Drolet, G. G., Middleton, E. M., Huemmrich, K. F., Hall, F. G., Amiro, B. D., Barr, A. G., Black, T. A., mcCaughey, H. A., & Margolis, H. A. (2008). Regional mapping of gross light-use efficiency using MODIS spectral indices. *Remote Sensing of Environment*, *112*, 3064−3078.

Field, C., Chapin, F., III, Matson, P., & Mooney, H. (1992). Responses of terrestrial ecosystems to the changing atmosphere: A resource-based approach. *Annual Review of Ecological Systems*, *23*, 201−235.

Field, C., & Mooney, H. A. (1986). The photosynthesis–nitrogen relationship in wild plants. In T. Givnish (Ed.), *On the economy of plant form and function* (pp. 22−55). Cambridge, U.K.: Cambridge Univ. Press.

Gamon, J. A., Filella, I., & Peñuelas, J. (Eds.). (1993). *The dynamic 531-nanometer reflectance signal: A survey of twenty angiosperm species* Rockville: American Society of Plant Physiologists.

Gamon, P. F., Penuelas, J., & Field, C. B. (1992). A narrow-waveband spectral index that tracks diurnal changes in photosynthetic efficiency. *Remote Sensing of Environment*, *41*, 35−44.

Garbulsky, M. F., Penuelas, J., Papale, D., & Filella, I. (2008). Remote estimation of carbon dioxide uptake by a Mediterranean forest. *Global Change Biology*, *14*, 2860−2867.

Hall, F. G., Hilker, T., Coops, N. C., Lyapustin, A., Huemmrich, F., Middleton, E., Margolis, H., Drolet, G., & Black, T. (2008). Multi-angle remote sensing of forest light use efficiency by observing PRI variation with canopy shadow fraction. *Remote Sensing of Environment*, *112*, 3201−3211.

Hall, F. G., Shimabukuro, Y. E., & Huemmrich, K. F. (1995). Remote sensing of forest biophysical structure using mixture decomposition and geometric reflectance models. *Ecologocial Applications*, *5*, 993−1013.

Hall, F. G., Huemmrich, K. F., Goetz, S. J., Sellers, P. J., & Nickeson, J. E. (1992). Satellite remote-sensing of surface-energy balance-success, failures and unresolved issues in FIFE. *Journal of Geophysical Research-Atmospheres*, *97*, 19061−19089.

Heinsch, F. A., Zhao, M. S., Running, S. W., Kimball, J. S., Nemani, R. R., Davis, K. J., Bolstad, P. V., Cook, B. D., Desai, A. R., Ricciuto, D. M., Law, B. E., Oechel, W. C., Kwon, H., Luo, H. Y., Wofsy, S. C., Dunn, A. L., Munger, J. W., Baldocchi, D. D., Xu, L. K., Hollinger, D. Y., Richardson, A. D., Stoy, P. C., Siqueira, M. B. S., Monson, R. K., Burns, S. P., & Flanagan, L. B. (2006). Evaluation of remote sensing based terrestrial productivity from MODIS using regional tower eddy flux network observations. *IEEE Transactions on Geoscience and Remote Sensing*, *44*, 1908−1925.

Hilker, T., Coops, N. C., Coggins, S., Wulder, M. A., Brown, M., Black, T. A., Nesic, Z., & Lessard, D. (2009). Detection of foliage conditions and disturbance from multi-angular high spectral resolution remote sensing. *Remote Sensing of Environment*, *113*, 421−434.

Hilker, T., Coops, N. C., Hall, F. G., Black, T. A., Chen, B., Krishnan, P., Wulder, M. A., Sellers, P. J., Middleton, E. M., & Huemmrich, K. F. (2008). A modeling approach for up-scaling gross ecosystem production to the landscape scale using remote sensing data. *Journal of Geophysical Research — Biogeosciences*, *113*, G03006.

Hilker, T., Coops, N. C., Hall, F. G., Black, T. A., Wulder, M. A., Nesic, Z., & Krishnan, P. (2008). Separating physiologically and directionally induced changes in PRI using BRDF models. *Remote Sensing of Environment*, *112*, 2777−2788.

Hilker, T., Coops, N. C., Nesic, Z., Wulder, M. A., & Black, A. T. (2007). Instrumentation and approach for unattended year round tower based measurements of spectral reflectance. *Computers and Electronics in Agriculture*, *56*, 72−84.

Hilker, T., Coops, N. C., Schwalm, C. R., Jassal, R. S., Black, T. A., & Krishnan, P. (2008). Effects of mutual shading of tree crowns on prediction of photosynthetic light-use efficiency in a coastal douglas-fir forest. *Tree Physiology*, *28*, 825−834.

Humphreys, E. R., Black, T. A., Morgenstern, K., Cai, T. B., Drewitt, G. B., Nesic, Z., & Trofymow, J. A. (2006). Carbon dioxide fluxes in coastal douglas-fir stands at different stages of development after clearcut harvesting. *Agricultural and Forest Meteorology*, *140*, 6−22.

Jassal, R. S., Black, T. A., Cai, T. B., Morgenstern, K., Li, Z., Gaumont-Guay, D., & Nesic, Z. (2007). Components of ecosystem respiration and an estimate of net primary productivity of an intermediate-aged douglas-fir stand. *Agricultural and Forest Meteorology*, *144*, 44−57.

Kaufman, Y. J., Tanre, D., et al. (1997). Operational remote sensing of tropospheric aerosol over land from EOS moderate resolution imaging spectroradiometer. *Journal of Geophysical Research*, *102*, 17051−17067.

Kljun, N., Kastner-Klein, P., Fedorovich, E., & Rotach, M. W. (2004). Evaluation of Lagrangian footprint model using data from wind tunnel convective boundary layer. *Agricultural and Forest Meteorology*, *127*, 189−201.

Levy, R. C., Remer, L., Mattoo, S., Vermote, E., & Kaufman, Y. J. (2007). Second-generation algorithm for retrieving aerosol properties over land from MODIS spectral reflectance. *Journal of Geophysical Research*, *112*, D13211. doi:10.1029/2006JD007811.

Li, X. W., & Strahler, A. H. (1985). Geometric–optical modeling of a conifer forest canopy. *IEEE Transactions on Geoscience and Remote Sensing*, *23*, 705−721.

Los, S. O., North, P. R. J., Grey, W. M. F., & Barnsley, M. J. (2005). A method to convert AVHRR normalized difference vegetation index time series to a standard viewing and illumination geometry. *Remote Sensing of Environment*, *99*, 400−411.

Lyapustin, A. I. (1999). Atmospheric and geometrical effects on land surface albedo. *Journal of Geophysical Research*, *104*, 4123−4143.

Lyapustin, A., & Knyazikhin, Yu. (2001). Green's function method in the radiative transfer problem. I: Homogeneous non-Lambertian surface. *Applied Optics*, *40*, 3495−3501.

Lyapustin, A., & Wang, Y. (2005). Parameterized code sharm-3D for radiative transfer over inhomogeneous surfaces. *Applied Optics*, *44*, 7602−7610.

Lyapustin, A., Wang, Y., & Frey, R. (2008). An automatic cloud mask algorithm based on time series of MODIS measurements. *Journal of Geophysical Research*, *113*, D16207. doi:10.1029/2007JD009641.

Lyapustin, A., & Wang, Y. (2009). The time series technique for aerosol retrievals over land from MODIS. In A. Kokhanovky, & G. De Leeuw (Eds.), *Satellite aerosol remote sensing over land* (pp. 69−99). : Springer Praxis Books978-3-540-69396-3.

Lyapustin, A., & Wang, Y. (2008). MAIAC — Multi-angle implementation of atmospheric correction for MODIS. *Algorithm Theoretical Basis Document, Ver.1.0, 77 pp.* Available at: http://neptune.gsfc.n asa.gov/bsb/subpages/index.php?section=Projects&content=SHARM, section MAIAC ATBD.

Martel, M. C., Margolis, H. A., Coursolle, C., Bigras, F. J., Heinsch, F. A., & Running, S. W. (2005). Decreasing photosynthesis at different spatial scales during the late growing season on a boreal cutover. *Tree Physiology*, *25*, 689−699.

Monteith, J. L. (1972). Solar-radiation and productivity in tropical ecosystems. *Journal of Applied Ecology*, *9*, 747−766.

Monteith, J. L. (1977). Climate and efficiency of crop production in Britain. *Philosophical Transactions of the Royal Society of London Series B-Biological Sciences*, *281*, 277−294.

Morgenstern, K., Black, T. A., Humphreys, E. R., Griffis, T. J., Drewitt, G. B., Cai, T. B., Nesic, Z., Spittlehouse, D. L., & Livingstone, N. J. (2004). Sensitivity and uncertainty of the carbon balance of a pacific northwest douglas-fir forest during an El Nino La Nina Cycle. *Agricultural and Forest Meteorology*, *123*, 201−219.

Pellegrini, L., Boni, P., & Carton, A. (2003). Hydrographic evolution in relation to neotectonics aided by data processing and assessment: Some examples from the Northern Apennines (Italy). *Quaternary International*, *101*, 211−217.

Peñuelas, J., Filella, I., & Gamon, J. A. (1995). Assessment of photosynthetic radiation-use efficiency with spectral reflectance. *New Phytologist*, *131*, 291−296.

Peñuelas, J., Filella, I., Gamon, J. A., & Field, C. (1997). Assessing photosynthetic radiation-use efficiency of emergent aquatic vegetation from spectral reflectance. *Aquatic Botany*, *58*, 307−315.

Peñuelas, J., Llusia, J., Pinol, J., & Filella, I. (1997). Photochemical reflectance index and leaf photosynthetic radiation-use-efficiency assessment in Mediterranean trees. *International Journal of Remote Sensing*, *18*, 2863−2868.

Prince, S. D., & Goward, S. N. (1995). Global primary production: A remote sensing approach. *Journal of Biogeography*, *22*, 815−835.

Rahman, A. F., Cordova, V. D., Gamon, J. A., Schmid, H. P., & Sims, D. A. (2004). Potential of modis ocean bands for estimating CO2 flux from terrestrial vegetation: a novel approach. *Geophysical Research Letters*, *31*.

Ross, J. K. (1981). *The radiation regime and architecture of plant stands*. The Hague: Dr. W. Junk Publishers.

Roujean, J. L., Leroy, M., & Deschamps, P. Y. (1992). A bidirectional reflectance model of the earths surface for the correction of remote-sensing data. *Journal of Geophysical Research-Atmospheres*, *97*, 20455−20468.

Running, S., Nemani, R., Heinsch, F., Zhao, M., Reeves, M., & Hashimoto, H. (2004). A continuous satellite-derived measure of global terrestrial primary production. *BioScience*, *54*, 547−560.

Running, S. W., Nemani, R. R., Heinsch, F. A., Zhao, M. S., Reeves, M., & Hashimoto, H. (2004). A continuous satellite-derived measure of global terrestrial primary production. *BioScience*, *54*, 547−560.

Schwalm, C. R., Black, T. A., Arniro, B. D., Arain, M. A., Barr, A. G., Bourque, C. P. A., Dunn, A. L., Flanagan, L. B., Giasson, M. A., Lafleur, P. M., Margolis, H. A., McCaughey, J. H., Orchansky, A. L., & Wofsy, S. C. (2006). Photosynthetic light use efficiency of three biomes across an east–west continental-scale transect in Canada. *Agricultural and Forest Meteorology*, *140*, 269−286.

Sellers, P.J. (Ed.) (1985). Vegetation-canopy spectral reflectance and biophysical processes In: Asrar, G. Editor, Theory and applications of optical remote sensing: Wiley, New York.

Sellers, P. J. (1987). Canopy reflectance, photosynthesis, and transpiration .2. The role of biophysics in the linearity of their interdependence. *Remote Sensing of Environment*, *21*, 143−183.

Sellers, P. J., Randall, D. A., Collatz, G. J., Berry, J. A., Field, C. B., Dazlich, D. A., Zhang, C., Collelo, G. D., & Bounoua, L. (1996). A revised land surface parameterization (Sib2) for Atmospheric GCMs .1. *Model Formulation. Journal of Climate*, *9*, 676−705.

Sims, D. A., & Gamon, J. A. (2002). Relationships between leaf pigment content and spectral reflectance across a wide range of species, leaf structures and developmental stages. *Remote Sensing of Environment*, *81*, 337−354.

Strahler, A., & Jupp, D. (1990). Modelling bidirectional reflectance of forests and woodlands using boolean models and geometric optics. *Remote Sensing of Environment*, *34*, 153−166.

Tan, B., Woodcock, C. E., Hu, J., Zhang, P., Ozdogan, M., Huang, D., Yang, W., Knyazikhin, Y., & Myneni, R. B. (2006). The impact of gridding artifacts on the local spatial properties of MODIS data: Implications for validation, compositing, and band-to-band registration across resolutions. *Remote Sensing of Environment*, *105*, 98−114.

Tucker, C. (1979). Red and photographic infrared linear combinations for monitoring vegetation. *Remote Sensing of Environment*, *8*, 127−150.

Turner, D. P., Ritts, W. D., Cohen, W. B., Gower, S. T., Zhao, M., Running, S. W., Wofsy, S. C., Urbanski, S., Dunn, A. L., & Munger, J. W. (2003). Scaling Gross Primary Production (GPP) over boreal and deciduous forest landscapes in support of MODIS GPP product validation. *Remote Sensing of Environment*, *88*, 256−270.

Van Den Eeckhaut, M., Poesen, J., Verstraeten, G., Vanacker, V., Moeyersons, J., Nyssen, J., & van Beek, L. P. H. (2005). The effectiveness of hillshade maps and expert knowledge in mapping old deep-seated landslides. *Geomorphology*, *67*, 351−363.

Vermote, E. F., & Kotchenova, S. (2008). Atmospheric correction for the monitoring of land surfaces. *Journal of Geophysical Research-Atmospheres*, 113.

Vermote, E. F., Tanre, D., Deuze, J. L., Herman, M., & Morcrette, J. J. (1997). Second simulation of the satellite signal in the solar spectrum, 6S: An overview. *IEEE Transactions on Geoscience and Remote Sensing*, *35*, 675−686.

Wanner, W., Li, X., & Strahler, A. H. (1995). On the derivation of kernels for kernel-driven models of bidirectional reflectance. *Journal of Geophysical Research-Atmospheres*, *100*, 21077−21089.

Wolfe, R. E., Roy, D. P., & Vermote, E. (1998). MODIS land data storage, gridding, and compositing methodology: Level 2 grid. *IEEE Transactions on Geoscience and Remote Sensing*, *36*, 1324−1338.